What Are the Relative Roles of Heating and Cooling in Generating Solar Wind Temperature Anisotropies?

B. A. Maruca,[1,2,*] J. C. Kasper,[2,1] and S. D. Bale[3,4]

[1]*Department of Astronomy, Harvard University, Cambridge, Massachusetts 02138, USA*
[2]*Harvard-Smithsonian Center for Astrophysics, Cambridge, Massachusetts 02138, USA*
[3]*Space Sciences Laboratory, University of California, Berkeley, California 94720, USA*
[4]*Department of Physics, University of California, Berkeley, California 94720, USA*

(Received 28 April 2011; published 11 November 2011)

Temperature anisotropy in the solar wind results from a combination of mechanisms of anisotropic heating (e.g., cyclotron-resonant heating and dissipation of kinetic Alfvén waves) and cooling (e.g., Chew-Goldberger-Low double-adiabatic expansion). In contrast, anisotropy-driven instabilities such as the cyclotron, mirror, and firehose instabilities limit the allowable departure of the plasma from isotropy. This study used data from the Faraday cups on the Wind spacecraft to examine scalar temperature and temperature components of protons. Plasma unstable to the mirror or firehose instability was found to be about 3–4 times hotter than stable plasma. Since anisotropy-driven instabilities are not understood to heat the plasma, these results suggest that heating processes are more effective than cooling processes at creating and maintaining proton temperature anisotropy in the solar wind.

DOI: 10.1103/PhysRevLett.107.201101 PACS numbers: 96.60.Vg, 95.30.Qd, 96.50.Ci, 96.50.Tf

Introduction.—Protons in the solar wind typically have an anisotropic velocity distribution function (VDF) [1,2] with separate temperatures $T_{\perp p}$ and $T_{\parallel p}$ in the directions perpendicular and parallel, respectively, to the local magnetic field **B** [3,4]. Anisotropic heating and cooling processes act preferentially on one temperature component and thus can cause $T_{\perp p} \neq T_{\parallel p}$. However, these deviations of temperature anisotropy $R_p \equiv T_{\perp p}/T_{\parallel p}$ from unity are limited by such mechanisms as anisotropy-driven instabilities [5,6] and thermalization due to Coulomb relaxation [7,8]. Characterizing the combined effect of these processes is important for understanding the dynamics of the solar wind [9] and of astrophysical plasmas in general [10,11].

A useful technique for studying solar wind temperature anisotropy is examining how R_p varies as a function of

$$\beta_{\parallel p} = \frac{n_p k_B T_{\parallel p}}{B^2/(2\mu_0)}, \tag{1}$$

which is the ratio of proton parallel pressure to magnetic pressure. Figure 1 shows the probability distribution $p(\beta_{\parallel p}, R_p)$ for solar wind measurements made by the Wind spacecraft at 1 A.U. The observed range of R_p values becomes narrower as $\beta_{\parallel p}$ increases. This effect has been associated with the action of anisotropy-driven instabilities, which can develop when R_p deviates too far from unity [6]. When active, these instabilities cause certain electromagnetic fluctuations to grow, which eventually scatters particles in phase space and ultimately drives the VDF toward isotropy. For $R_p < 1$ and $\beta_{\parallel p} \gtrsim 1$, the firehose instability can be triggered; for $R_p > 1$, the mirror and cyclotron instabilities can be active [3,6,12–14].

The growth rate γ of an instability is defined as the growth rate of its fastest-growing wave mode. Thus, an instability is described as "active" if $\gamma > 0$ (i.e., if at least some wave modes are growing). Since the growth rates of anisotropy-driven instabilities are most dependent on $\beta_{\parallel p}$

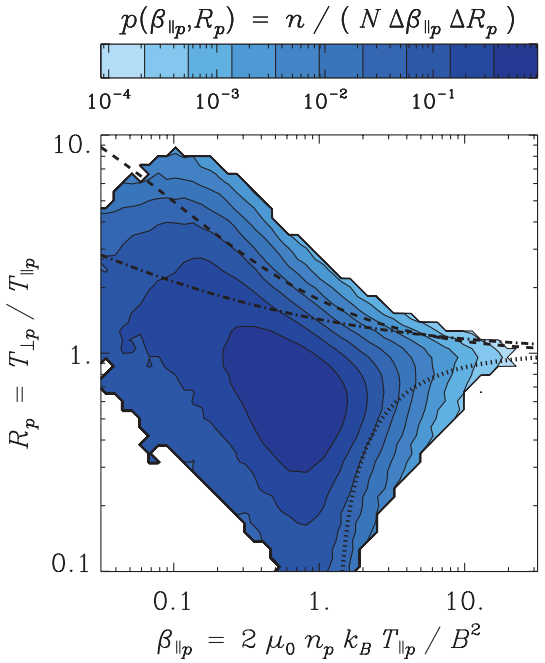

FIG. 1 (color). The distribution $p(\beta_{\parallel p}, R_p)$ in the solar wind at 1 A.U. The overlaid curves are thresholds for the oblique firehose (dotted), mirror (dashed), and cyclotron (dot-dashed) instabilities [12]. As $\beta_{\parallel p}$ increases the plasma is restricted to a narrower range of R_p.

and R_p, a common analysis technique thereof is considering contours of constant γ in the $(\beta_{\parallel p}, R_p)$ plane. For each instability, these contours move progressively out from the $R_p = 1$ axis for progressively larger values of γ (e.g., cf. [12]). The contour corresponding to $\gamma = 0$ can be thought of as the instability ''threshold'' since it separates the region of the $(\beta_{\parallel p}, R_p)$ plane for which the instability is active ($\gamma > 0$) from the region where it is not ($\gamma < 0$). However, for ease of computation, the nearby contour $\gamma = 10^{-3}\Omega_p$ (where Ω_p is the proton angular gyrofrequency) is typically used instead of $\gamma = 0$.

The overlaid curves in Fig. 1 are thresholds for the cyclotron, mirror, and firehose instabilities and were derived by using the linearized Vlasov equation [12]. The decrease in $p(\beta_{\parallel p}, R_p)$ near these thresholds indicates the action of these instabilities. Additionally, a prior study reported enhanced magnetic fluctuations in plasma near these thresholds, which provides further evidence that these instabilities are driving the growth of waves [15].

Plasma near a threshold is sometimes referred to as being ''marginally'' unstable to the corresponding instability: The instability growth rate γ, though positive, is quite small. Plasma can exist with $\gamma > 0$ for a time on the order of γ^{-1}. For the solar wind at 1 A.U., the threshold condition $\gamma = 10^{-3}\Omega_p$ typically corresponds to a time of hundreds or thousands of minutes, which is much shorter than the expansion time (i.e., days).

In order for $p(\beta_{\parallel p}, R_p)$ in Fig. 1 to extend up to and slightly beyond the instability thresholds, ongoing processes must be acting to counteract the isotropizing effects of the instabilities. The most obvious candidates are anisotropic heating and cooling processes, since they directly affect the temperature components. The most frequently cited anisotropic cooling mechanism is Chew-Goldberger-Low double-adiabatic expansion [16], which causes $T_{\perp p}$ to decrease more quickly than $T_{\parallel p}$ as plasma expands. Chew-Goldberger-Low expansion can account for trends in R_p and $\beta_{\parallel p}$ as functions of distance from the Sun [17,18] and for the extreme temperature anisotropies encountered in the lunar wake [19]. Conversely, perpendicular heating has been associated with the cyclotron-resonant absorption of Alfvén waves [4,20,21]. Likewise, studies have identified the Landau damping of kinetic Alfvén waves as a source both of perpendicular heating [22,23] and of parallel heating (for $\beta_{\parallel p} \gtrsim 1$) [11,24,25].

Anisotropy-driven instabilities themselves are not understood to appreciably heat or cool the plasma (cf. [26]). Since the free energy that drives these instabilities is associated with $R_p \neq 1$, their ultimate effect is to bring $T_{\perp p}$ and $T_{\parallel p}$ closer to equality while conserving T_p. Thus, comparing the temperatures of stable and unstable plasma gauges the relative roles of anisotropic heating and cooling in the plasma prior to the instability's onset. For example, if T_p is elevated in marginally unstable plasma, anisotropic heating was more active than cooling; if T_p is depressed, anisotropic cooling was more active. This Letter reports the results of such an analysis, which includes an investigation of how T_p and its components $T_{\perp p}$ and $T_{\parallel p}$ vary across the $(\beta_{\parallel p}, R_p)$ plane.

Observations.—This study primarily makes use of data from the Wind spacecraft's two Faraday cups, which are part of the Solar Wind Experiment [27]. Over the course of each three-second rotation of the Wind spacecraft, each cup makes 20 measurements of the current produced by solar wind ions in a given energy-per-charge range. An ''ion spectrum'' consists of these measurements made over several rotations (up to 31), each of which has a different energy-per-charge range. Software is used to fit bi-Maxwellian VDFs for protons and α particles to each spectrum [28]. As part of the fitting process, measurements of **B** from another Wind instrument, the Magnetic Field Investigation [29], are used to separate the parallel and perpendicular temperature components.

Recently, this software has undergone a series of revisions. The merging of Magnetic Field Investigation data and Solar Wind Experiment ion spectra has been significantly improved to more effectively utilize the higher cadence of the former. Additionally, the fitting algorithm itself has been modified to better exclude ion beams [30] (when present) so that the derived bulk parameters are more representative of the core VDFs. A full description and analysis of these revisions will be presented in a forthcoming article.

The revised software was used to analyze the 4.8×10^6 Solar Wind Experiment ion spectra recorded from late 1994 (i.e., launch) to mid-2010, but only 37% of these met the three criteria for use in this study. First, the uncertainties in the derived thermal speeds were required to be $<10\%$. Second, in order to avoid magnetospheric plasma and solar wind plasma that had been modified by the terrestrial foreshock, the Wind spacecraft was required to have been far from the Earth's bow shock. Finally, to avoid the effects of Coulomb relaxation, the Coulomb collisional age (i.e., the number of thermalization time scales that elapsed as the plasma traveled from the Sun to the Wind spacecraft [8]) was required to be ≤ 0.1.

Analysis.—To generate Figs. 1–3 in this Letter, the selected observations were divided into a 50×50 grid of logarithmically spaced bins in the $(\beta_{\parallel p}, R_p)$ plane. The number of observations n in each bin was calculated, and bins with $n < 50$ were discarded. For Fig. 1, the probability distribution $p(\beta_{\parallel p}, R_p)$ was estimated for each bin by dividing n by the bins's widths $\Delta\beta_{\parallel p}$ and ΔR_p and by the total number of spectra. Each plot in Figs. 2 and 3 shows, for each of its bins, the median value of the parameter listed in the plot's title. Note that the grids in Figs. 1–3 have been interpolated into contours.

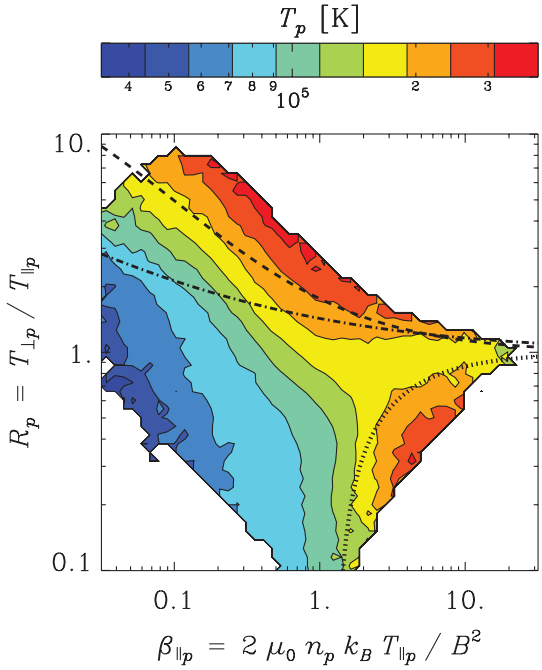

FIG. 2 (color). Plot of $T_p = (2T_{\perp p} + T_{\parallel p})/3$ over the $(\beta_{\parallel p}, R_p)$ plane. The curves indicate theoretical instability thresholds (see Fig. 1). The regions where the median T_p is highest occur beyond the instability thresholds.

As stated in the introduction, the alignment of the contours of $p(\beta_{\parallel p}, R_p)$ in Fig. 1 with the thresholds of the firehose and mirror instabilities strongly suggests that they are acting in solar wind plasma. However, this figure (like similar figures in Refs. [12,15]) curiously shows that the contours of $p(\beta_{\parallel p}, R_p)$ are not well aligned with the cyclotron instability threshold. This holds true even at $\beta_{\parallel p} \lesssim 2$, where the cyclotron instability theoretically places a stronger upper bound on $R_p > 1$ than the mirror instability. While the exact cause of this effect remains unknown, it may be related to the mirror instability (unlike the cyclotron instability) being nonpropagating [15,26], which could make it more efficient at scattering particles in phase space. Additionally, magnetic turbulence over a wide range of size scales tends to be aligned perpendicular (rather than parallel) to **B** [23,31], which may hasten the onset of the mirror instability.

Figure 2 shows T_p over the $(\beta_{\parallel p}, R_p)$ plane. Beyond the tendency for T_p to grow with $\beta_{\parallel p}$, which is expected since $\beta_{\parallel p} \propto T_{\parallel p}$, the highest T_p values occur in two regions: one near the mirror instability threshold and the other near the firehose instability threshold. Even at high $\beta_{\parallel p}$, these regions have median T_p values that are 3–4 times higher than that of the region between them (near $R_p = 1$), which is consistent with an earlier suggestions of this effect by Ref. [32]. Additionally, the high-T_p region at $R_p > 1$ is more aligned with the mirror instability threshold than the cyclotron instability threshold, which provides further evidence that (at 1 A.U.) the mirror instability is more active in limiting $R_p > 1$.

Plots of $T_{\perp p}$ and $T_{\parallel p}$ over the $(\beta_{\parallel p}, R_p)$ plane are shown in Fig. 3. These plots, when considered alongside Fig. 2, indicate that the enhanced T_p near the mirror instability threshold is almost entirely due to increased $T_{\perp p}$ and that

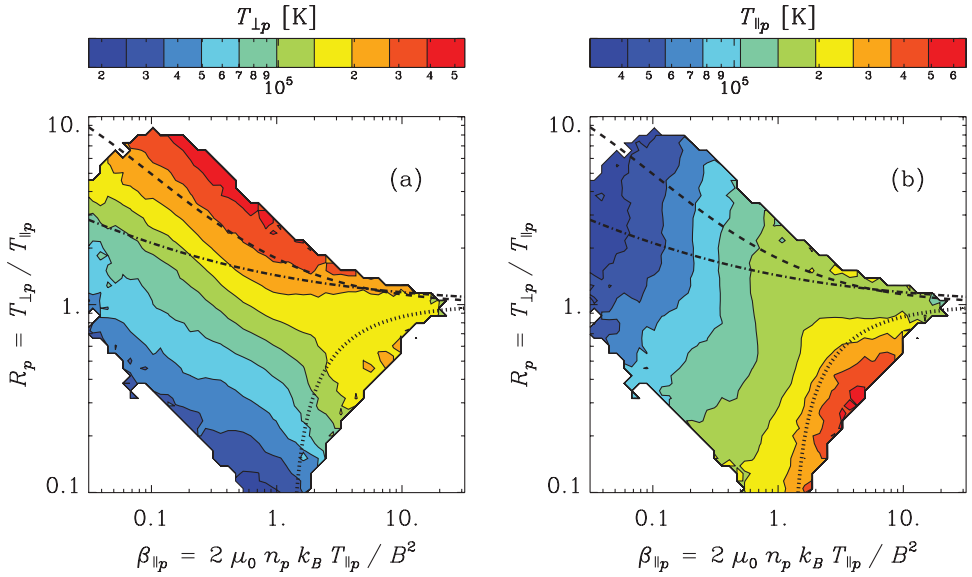

FIG. 3 (color). Plots of $T_{\perp p}$ (a) and $T_{\parallel p}$ (b) over the $(\beta_{\parallel p}, R_p)$ plane. The curves indicate theoretical instability thresholds (see Fig. 1). The enhancements in T_p seen in Fig. 2 are mainly in $T_{\perp p}$ for plasma beyond the mirror threshold and in $T_{\parallel p}$ for plasma beyond the firehose threshold. Slight enhancements can also be seen in $T_{\perp p}$ near the firehose instability threshold and in $T_{\parallel p}$ near the mirror instability threshold.

the enhanced T_p near the firehose instability threshold is almost entirely due to increased $T_{\|p}$. Conceivably, deviations in R_p from unity could stem from a decrease in one of the two temperature components. However, the plots in Fig. 3 show no evidence that $T_{\perp p}$ is depressed near the firehose instability threshold or that $T_{\|p}$ is depressed near the mirror instability threshold. In fact, in both of these cases, a slight enhancement is evident (especially at $\beta_{\|p} \gtrsim 1$).

Discussions and conclusion.—The preceding analysis of Wind data shows that (relative to stable plasma) the median T_p value is 3–4 times higher in plasma unstable to the mirror or firehose instability. Though increases in both $T_{\perp p}$ and $T_{\|p}$ are seen with both instabilities, virtually all of the enhancement is in $T_{\perp p}$ for the mirror instability and in $T_{\|p}$ for the firehose instability.

Since anisotropy-driven instabilities themselves are not believed to heat plasma, these temperature enhancements most likely result from processes that preferentially heat one of the temperature components until the protons become unstable. While, in principle, anisotropic cooling processes could drive R_p far enough from unity to trigger an instability, this analysis finds no evidence that T_p, $T_{\perp p}$, or $T_{\|p}$ is depressed in unstable plasma. Instead, for $\beta_{\|p} \gtrsim 1$, $T_{\perp p}$ and $T_{\|p}$ seem to be slightly elevated near the firehose and mirror instability threshold, respectively. This may be indicative of perpendicular and parallel heating processes happening simultaneously (but at different rates) or of the initial stages of the instabilities isotropizing the plasma.

Even though the growth rate of the cyclotron instability is higher than that of the mirror instability for $\beta_{\|p} \lesssim 2$, the contours of $p(\beta_{\|p}, R_p)$, T_p, and $T_{\perp p}$ are much better aligned with the threshold of the mirror instability. This provides further support for the conclusion of Refs. [12,15] that the mirror instability may be more active in limiting $R_p > 1$ in the solar wind than the cyclotron instability.

J. C. K. and B. A. M. thank S. Cranmer, S. P. Gary, M. L. Stevens, R. Narayan, and J. Raymond for discussions. Analysis of Wind observations is supported by NASA Grant No. NNX08AW07G. This research has made use of the SAO/NASA Astrophysics Data System (ADS).

*bmaruca@cfa.harvard.edu

[1] A. Eviatar and M. Schulz, Planet. Space Sci. **18**, 321 (1970).
[2] E. Marsch *et al.*, J. Geophys. Res. **87**, 52 (1982).
[3] J. C. Kasper, A. J. Lazarus, and S. P. Gary, Geophys. Res. Lett. **29**, 20 (2002).
[4] J. C. Kasper *et al.*, Astrophys. J. **660**, 901 (2007).
[5] S. J. Schwartz, Rev. Geophys. Space Phys. **18**, 313 (1980).
[6] S. P. Gary, *Theory of Space Plasma Microinstabilities* (Cambridge University Press, Cambridge, England, 1993).
[7] E. Marsch and H. Goldstein, J. Geophys. Res. **88**, 9933 (1983).
[8] J. C. Kasper, A. J. Lazarus, and S. P. Gary, Phys. Rev. Lett. **101**, 261103 (2008).
[9] J. A. Klimchuk, Sol. Phys. **234**, 41 (2006).
[10] P. Sharma *et al.*, Astrophys. J. **667**, 714 (2007).
[11] A. A. Schekochihin *et al.*, Astrophys. J. Suppl. Ser. **182**, 310 (2009).
[12] P. Hellinger *et al.*, Geophys. Res. Lett. **33**, 9101 (2006).
[13] S. P. Gary and M. A. Lee, J. Geophys. Res. **99**, 11 297 (1994).
[14] S. P. Gary *et al.*, Geophys. Res. Lett. **28**, 2759 (2001).
[15] S. D. Bale *et al.*, Phys. Rev. Lett. **103**, 211101 (2009).
[16] G. F. Chew, M. L. Goldberger, and F. E. Low, Proc. R. Soc. A **236**, 112 (1956).
[17] E. Marsch and A. K. Richter, J. Geophys. Res. **89**, 6599 (1984).
[18] L. Matteini *et al.*, Geophys. Res. Lett. **34**, 20 105 (2007).
[19] D. Clack *et al.*, Geophys. Res. Lett. **31**, L06812 (2004).
[20] J. V. Hollweg and P. A. Isenberg, J. Geophys. Res. **107**, 1147 (2002).
[21] E. Marsch and C.-Y. Tu, J. Geophys. Res. **106**, 8357 (2001).
[22] F. Sahraoui *et al.*, Phys. Rev. Lett. **102**, 231102 (2009).
[23] F. Sahraoui *et al.*, Phys. Rev. Lett. **105**, 131101 (2010).
[24] E. Quataert, Astrophys. J. **500**, 978 (1998).
[25] B. D. G. Chandran *et al.*, Astrophys. J. **720**, 503 (2010).
[26] D. J. Southwood and M. G. Kivelson, J. Geophys. Res. **98**, 9181 (1993).
[27] K. W. Ogilvie *et al.*, Space Sci. Rev. **71**, 55 (1995).
[28] J. C. Kasper *et al.*, J. Geophys. Res. **111**, 3105 (2006).
[29] R. P. Lepping *et al.*, Space Sci. Rev. **71**, 207 (1995).
[30] W. C. Feldman *et al.*, J. Geophys. Res. **78**, 2017 (1973).
[31] Y. Narita *et al.*, Geophys. Res. Lett. **38**, L05101 (2011).
[32] Y. Liu *et al.*, J. Geophys. Res. (Space Phys.) **111**, 1102 (2006).